Near Surface Geophysics, 2006, 253-263

Fresnel reflection coefficients for GPR-AVA analysis and detection of seawater and NAPL contaminants

José M. Carcione[1*], Davide Gei[1], Marco A.B. Botelho[2], Ana Osella[3] and Matias de la Vega[3]

[1]*Istituto Nazionale di Oceanografia e di Geofisica Sperimentale, Borgo Grotta Gigante 42c, 34010 Sgonico, Trieste, Italy*
[2]*Instituto de Geosciências, Campus Universitário de Ondina, Universidade Federal da Bahia, Salvador-BA, Brazil*
[3]*Departamento de Física, Facultad de Ciencias Exactas y Naturales, Universidad de Buenos Aires, Ciudad Universitaria, Pab. 1, 1428 Buenos Aires, Argentina*

Received December 2004, revision accepted November 2005

ABSTRACT

We obtain the transverse electric (TE) and transverse magnetic (TM) Fresnel reflection coefficients for different interfaces in the subsoil: air/fresh-water, air/seawater, fresh-water/seawater, air/NAPL (non-aqueous phase liquid), NAPL/water and water/NAPL. We consider a range of NAPL saturations, where the complementary fluid is water with 0.65 ppt (parts per thousand) of NaCl. The common feature is that the TM mode (parallel polarization) has a negative anomaly and the TE mode (perpendicular polarization) has a positive anomaly. For the cases studied in this work, pseudo-Brewster angles appear beyond 40° for the air/NAPL and NAPL/water interfaces and at near offsets (below 40°) for the water/NAPL interface. Pseudo-critical angles are present for the water/NAPL interface. Besides the reflection strength, the phase angle can be used to discriminate between low- and high-conductivity NAPL, when the properties of the upper medium are known. A wavenumber–frequency domain method is used to compute the reflection coefficient and phase angle from synthetic radargrams. This method and the curves can be used to interpret the amplitude variations with angle (AVA) of reflection events in radargrams obtained with ground-penetrating radar (GPR).

INTRODUCTION

The flow of seawater into fresh-water aquifers, and the injection of brine into the subsurface through hydrocarbon production wells, constitutes a major problem affecting the quality of industrial and domestic water supplies. Another problem is the contamination of the subsoil with hydrocarbons. Contaminants may exist in the gas phase, in the aqueous phase, and/or as a separate, immiscible liquid phase (i.e. non-aqueous phase liquids: NAPLs). Light NAPLs (LNAPLs) consist of a solution of organic compounds (e.g. petroleum hydrocarbons) which is less dense than water and forms a layer that floats on the surface of the groundwater table. On the other hand, dense NAPLs (DNAPLs) consist of a solution of organic compounds (e.g. chlorinated hydrocarbons) that is denser than water. DNAPLs sink to the bottom of the aquifer.

Ground-penetrating radar (GPR) and electrical methods have been applied with success to locate the fresh-water/seawater interface in the subsoil (e.g. Pereira *et al*. 2003), and to map the location of NAPL spills on the basis of the dielectric and electrical properties (Greenhouse *et al*. 1993; Benson 1995; Daniels *et al*. 1995; Carcione *et al*. 2000; Carcione and Seriani 2000; Osella *et al*. 2002; de la Vega *et al*. 2003; Carcione *et al*. 2003). In fact, at radar frequencies, NAPLs have, in general, lower permittivity and conductivity than groundwater. However, significant changes in the electrical properties of hydrocarbon spills can occur as a result of bacterial bio-degradation. In this case, the hydrocarbon spill becomes highly conductive (Sauck 2000).

Several factors determine the GPR response, namely, the transmitter–receiver configuration, the survey direction, the reflection coefficient and orientation of the target, the properties of the overlying layers, etc. (e.g. Roberts and Daniels 1996; Lutz *et al*. 2003). Besides the reflection strength and traveltime (e.g. Botelho *et al*. 2003), the presence of seawater and the NAPL saturation can be estimated by analysing the amplitude variations of the reflection event (Lehmann 1996; Baker 1998; Reppert *et al*. 2000). Zeng *et al*. (2000) presented synthetic AVO computations by varying the electromagnetic properties of a layer over a half-space. They performed the analysis in the space–time domain. In this paper, we calculate the Fresnel reflection coefficients for different cases, and obtain the AVA curves in the

* jcarcione@inogs.it

© 2006 European Association of Geoscientists & Engineers

frequency–wavenumber domain, which can be compared directly with the Fresnel coefficients.

The AVA curves can be used to interpret reflection events in radargrams obtained with GPR. In particular, it is important to analyse the Brewster angle (Born and Wolf 1964), which is observed in the TM reflection coefficient, and the type of AVA anomaly (positive or negative). In fact, the Brewster angle does not occur in the subsoil, since the constituent media are not perfect dielectrics, i.e. the media are lossy (Carcione 2001). However, we may consider a minimum in the absolute value of the reflection coefficient as a pseudo-Brewster angle, which can also be useful to characterize the media. The same argument can be applied to critical angles, because they are rare exceptions in lossy media (Carcione 2001). The term pseudo-critical angle is applied in this case. Generally, for low-to-high permittivity interfaces, similar shapes of the Fresnel coefficients are obtained, where a pseudo-Brewster angle will be present for the TM mode. On the other hand, for high-to-low permittivity interfaces, a pseudo-critical angle occurs for the TM and TE modes.

THEORY

The subsoil is composed of a mixture of sand, silt and clay, air, water and contaminant. A number of models have been proposed to determine the electromagnetic properties of composites. We use the complex refractive index method (CRIM) (e.g. Schön 1996), for which the complex permittivity is given by

$$\varepsilon^* = \left(\sum_\alpha f_\alpha \sqrt{\varepsilon_\alpha} \right)^2, \tag{1}$$

where indicates the type of phase, f and e and are the volume fraction and complex permittivity of phase . If denotes the porosity and the subscripts 's', 'a', 'w' and 'NAPL' denote solid grain, air, water and contaminant, the respective fractions are given by f_s = 1 - , f = (1 - S_w - S_{NAPL}), f_W = S_W and f_{NAPL} = S_{NAPL} , where S_a indicates the saturation of phase . Then, (1) becomes

$$\sqrt{\varepsilon^*} = (1-\phi)\sqrt{\varepsilon_s} + \phi(1 - S_w - S_{NAPL})\sqrt{\varepsilon_a} + \phi S_w \sqrt{\varepsilon_w} + \phi S_{NAPL} \sqrt{\varepsilon_{NAPL}}. \tag{2}$$

This model is very simple and easy to implement. It uses the ray approximation in dielectrics. (The traveltime in phase is inversely proportional to the electromagnetic velocity, which in turn is inversely proportional to the square root of the permittivity.)

For NAPL, the complex permittivity has the form,

$$\varepsilon_{NAPL} = \varepsilon + \frac{i\sigma}{\omega}, \tag{3}$$

where is the DC conductivity, $w = 2\pi f$ is the angular frequency, and f is the frequency. The complex dielectric properties of water are described by the Cole–Cole model,

$$\varepsilon_w = \varepsilon^\infty + \frac{\varepsilon^0 - \varepsilon^\infty}{1-(i\omega\tau)^q} + \frac{i\sigma}{\omega} \tag{4}$$

(Cole and Cole 1941; Taherian *et al*. 1990), where

$^0 = 80.1\ _0$, $^\infty = 4.23\ _0$, = 9.3 ps, $q = 0.987$

(Schön 1996). Equation (4) is a generalization of the Debye model, for which q =1 (Debye 1929).

The TM and TE generalized Fresnel reflection coefficients are given by

$$R_{TM} = \frac{n_2 \cos\theta_I - n_1 \cos\theta_T}{n_2 \cos\theta_I + n_1 \cos\theta_T} \tag{5}$$

and

$$R_{TE} = \frac{n_1 \cos\theta_I - n_2 \cos\theta_T}{n_1 \cos\theta_I + n_2 \cos\theta_T} \tag{6}$$

(Born and Wolf 1964), where $_I$ and $_T$ are the angles of incidence and refraction, and n_1 and n_2 are the refractive indices of the upper and lower medium, respectively (see Fig. 1). The preceding equations are generalizations of Fresnel equations to the conducting case.

The refractive index is related to the permittivity by

$$n^2 = \frac{\varepsilon^*}{\varepsilon_0}, \tag{7}$$

where $_0 = 8.85 \times 10^{-12}$ F/m, and we have assumed that the magnetic permeability is that of a vacuum. (Note that $^*/_0$ is termed dielectric constant.) Moreover, Snell's law relates the angles of incidence and refraction as follows:

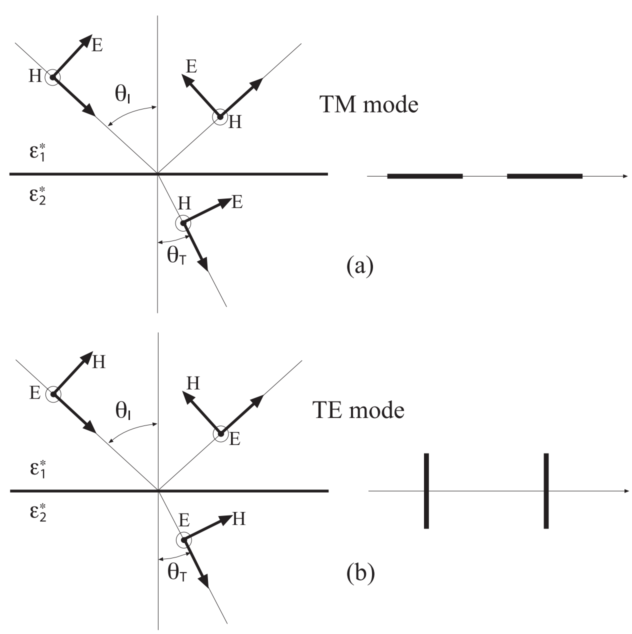

FIGURE 1
The reflection-refraction problem and the corresponding top view of the GPR antenna configurations (diagrams on the right-hand side). (a) Parallel endfire (TM mode, parallel polarization). (b) Perpendicular broadside (TE mode, perpendicular polarization).

© 2006 European Association of Geoscientists & Engineers, *Near Surface Geophysics, 2006,* **4**, 253-263

$$\frac{n_1}{\sin\theta_T} = \frac{n_2}{\sin\theta_I}. \quad (8)$$

The Brewster angle occurs for lossless media when the numerator of R_{TM} is zero, i.e.

$$\tan\theta_B = \sqrt{\frac{\varepsilon_2}{\varepsilon_1}}. \quad (9)$$

When we refer to lossless media, we consider that the effective conductivity is zero, with the effective permittivity and conductivity given by Re(*) and ωIm(*), where * is given by (1), and Re and Im denote real and imaginary parts, respectively.

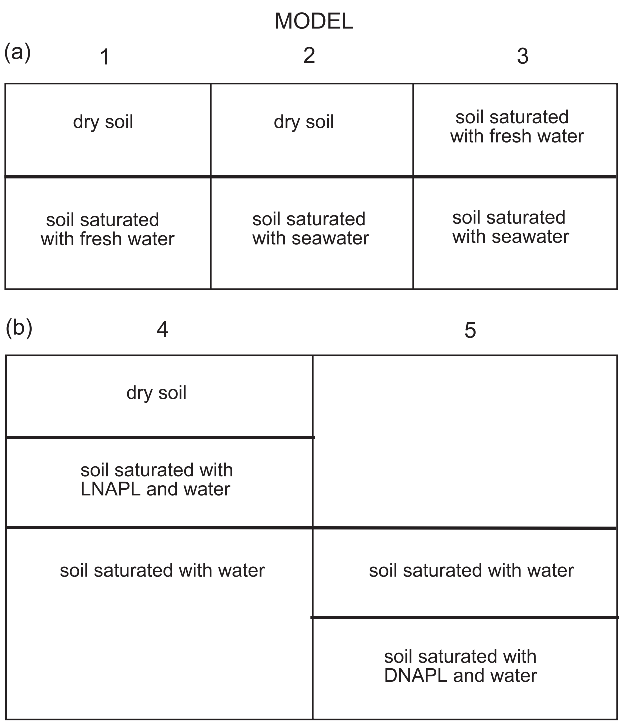

FIGURE 2
Diagram showing the interfaces (models 1 to 5) considered in this work, where (a) is the case of a coastal aquifer, and (b) is the case of soil contamination by NAPL.

TABLE 1
Electromagnetic properties. (*) 100 MHz, e_0 = 8.85 10^{-12} F/m

Medium	($_0$)	(S/m)
Grain	6.7	0
Air	1	0
Fresh water	80	0
Salt water*	80.1	0.1
Seawater*	80.1	5
NAPL-1	2	10^{-6}
NAPL-2	2	1

CALCULATION OF THE REFLECTION COEFFICIENTS

The interfaces (models 1 to 5) considered in this work are shown in Fig. 2, where (a) corresponds to the case of terrestrial fresh water interacting with seawater in coastal aquifers and (b) corresponds to a floating hydrocarbon spill. We assume the material properties given in Table 1. The properties of the grains which form the soil are assumed to be those of quartz. The relative permittivity of quartz is assumed to be greater than the commonly tabulated value of 4.5. This takes into account the presence of electrochemical effects by considering a wetted matrix. These effects are associated with the interaction of the rock/water interface; once this has been fully established through the adsorption of approximately 1 nm of water, the magnitude of the electrochemical effects are modelled (Knight and Endres 1990). Salt water has conductivity 0.1 S/m for a salinity of 0.65 ppt of NaCl and 5 S/m for a salinity of 35 ppt of NaCl (seawater) (Carcione *et al*. 2003). LNAPL and DNAPL have different densities but have the same electromagnetic properties. The difference is the location with respect to the water table (see Fig. 2). The increase in the conductivity of the hydrocarbon spill due to bio-degradation is modelled with high-conductivity NAPL, although this is an idealization of the real situation (Sauck 2000). The conductivities of NAPL are 10^{-6} S/m (NAPL-1) and 1 S/m (NAPL-2) before and after bio-degradation, respectively. In all the calculations, the reference frequency is f = 100 MHz and the soil porosity is 50%.

Figure 3 shows (a) the TM and (b) the TE Fresnel coefficients versus angle of incidence for the air/water interface (model 1) and the air/seawater interface (model 2). The pseudo-Brewster angle occurs at nearly 70° for the TM case. Beyond this angle the reflection coefficient becomes negative. The AVA anomaly is negative for the TM case and positive for the TE case, i.e. the reflection coefficients decrease and increase with increasing angle, respectively. The magnitude of the reflection coefficient is higher for seawater. The Fresnel coefficients for the fresh-water/seawater interface (model 3) are shown in Fig. 4. The qualitative features are similar to those of Fig. 3. This fact may lead to ambiguous interpretations. Fortunately, the type of fluid and saturation in the upper layer can also be determined on the basis of the traveltime of the reflection hyperbola.

Let us consider an interface at depth z and an offset x. The (two-way) traveltime difference between a dry soil (S_w = 0) and a partially saturated soil ($S_w \neq 0$) is

$$\Delta T = \phi S_w \sqrt{\mu_0}\left(\sqrt{\varepsilon_w} - \sqrt{\varepsilon_a}\right)\sqrt{x^2 + 4z^2}, \quad (10)$$

where $\mu_0 = 4\pi \times 10^{-7}$ H/m, and the subscripts ‘w’ and ‘a’ denote fresh water and air, respectively. We obtain

$$\Delta T = 0.26\phi S_w \sqrt{x^2 + 4z^2}, \quad (11)$$

where ΔT is given in ns and the distances in cm.

© 2006 European Association of Geoscientists & Engineers,

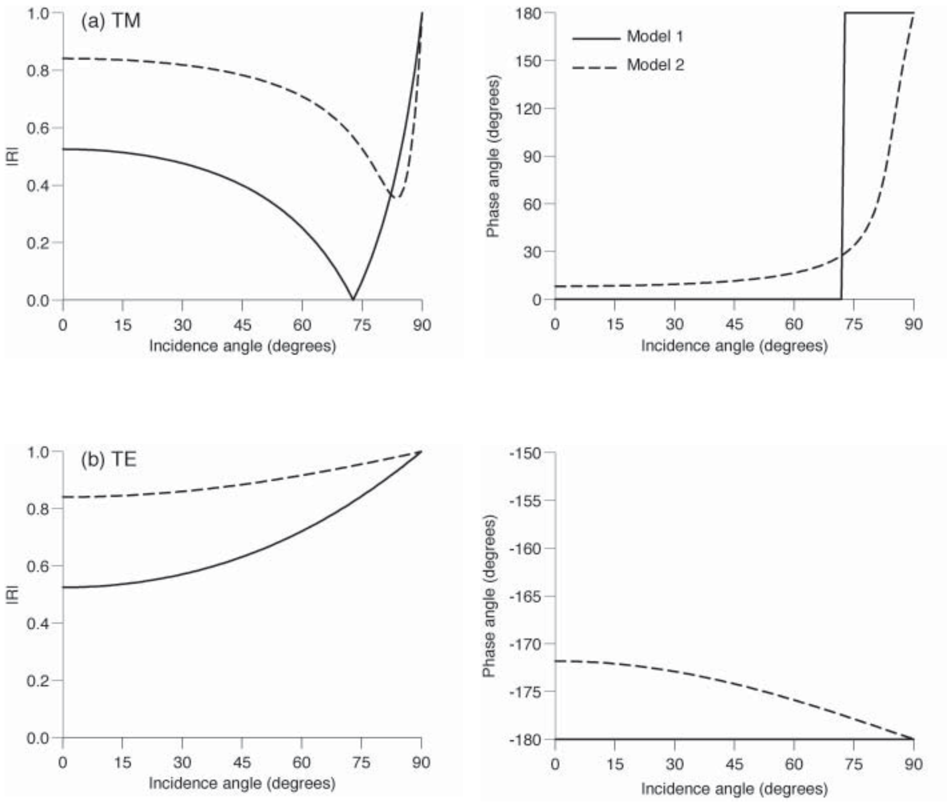

FIGURE 3
(a) TM and (b) TE Fresnel coefficients versus angle of incidence for model 1 (dry-soil/fresh-water interface) and model 2 (dry-soil/seawater interface).

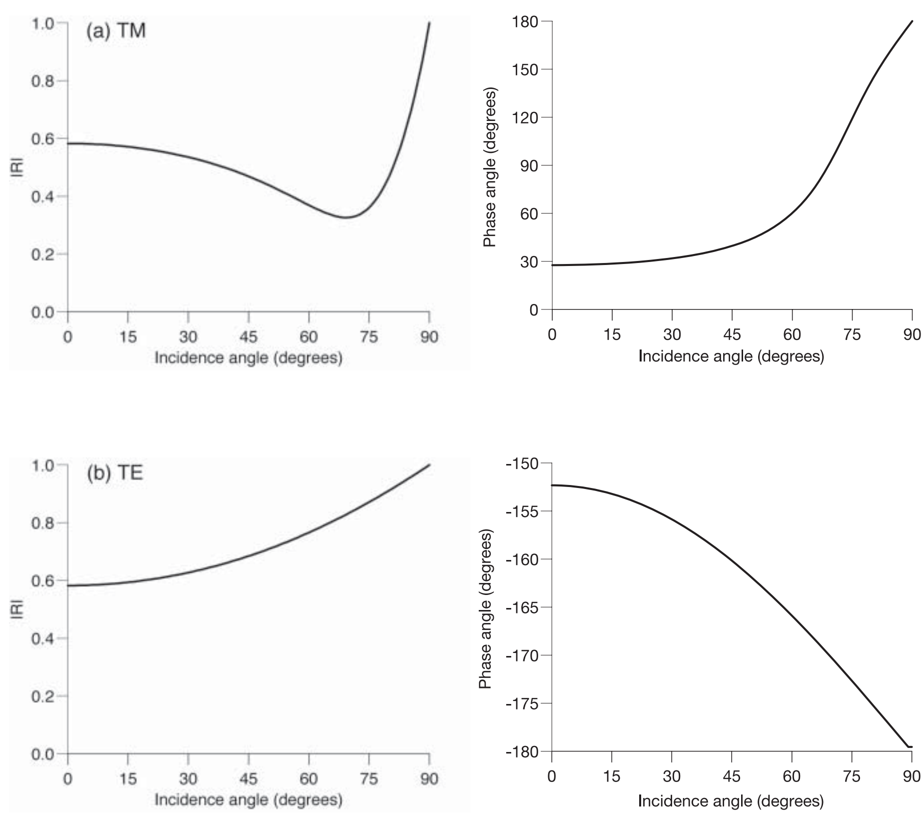

FIGURE 4
(a) TM and (b) TE Fresnel coefficients versus angle of incidence for model 3 (fresh-water/seawater interface).

© 2006 European Association of Geoscientists & Engineers, *Near Surface Geophysics, 2006,* **4**, 253-263

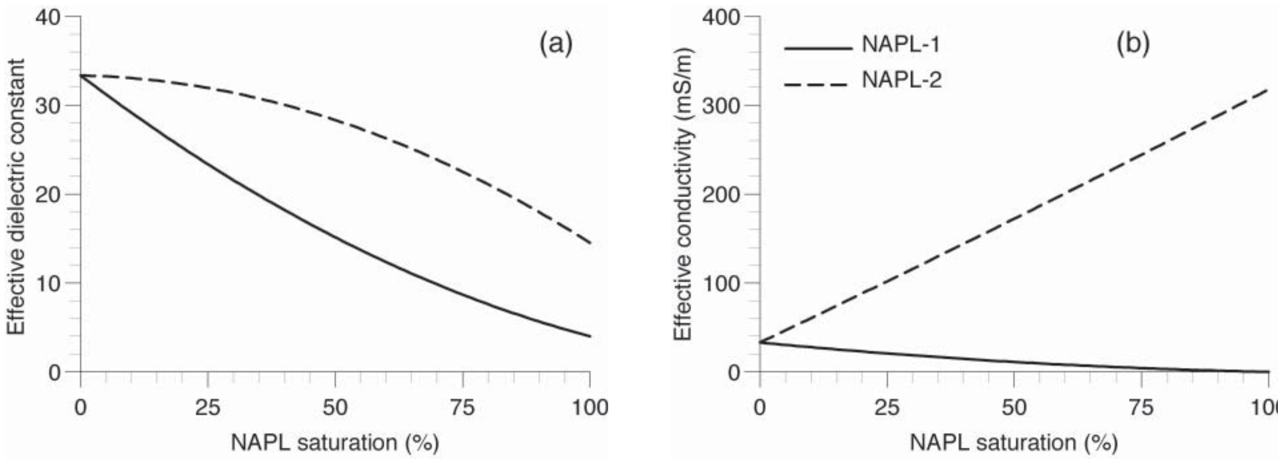

FIGURE 5
(a) Effective dielectric constant and (b) effective conductivity versus NAPL saturation. The other saturating fluid is salt water.

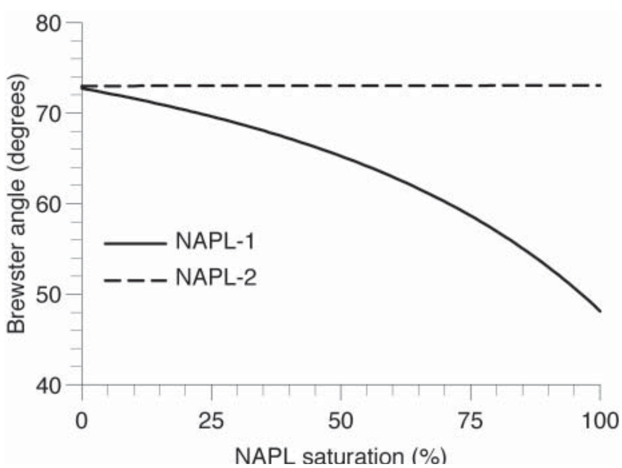

FIGURE 6
Brewster angle versus NAPL saturation for the dry soil/NAPL interface (model 4). The other saturating fluid is salt water.

If $x = 1$ m, $z = 0.5$ m, $= 0.5$, we obtain $\Delta T = 9$ ns for $S_w = 0.5$ and $\Delta T = 18$ ns for $S_w = 1$. Note that the difference in traveltime depends on and S_w, so the porosity should be known in order to determine the saturation.

We now consider the case when the upper medium is dry soil and the lower medium is the same soil partially saturated with 0.65 ppt NaCl water (salt water) and NAPL (model 4, upper interface; see Fig. 2b). The graphs of effective dielectric constant and effective conductivity versus NAPL saturation are shown in Fig. 5(a and b), respectively. The higher permittivity and conductivity for NAPL-2 causes a strong reflectivity of the top of the hydrocarbon plume and significant energy losses through the plume. This explains the characteristic response observed in radargrams of bio-degraded hydrocarbon spills. Figure 6 shows the pseudo-Brewster angle versus NAPL saturation (equation (9)). The Brewster angle appears at long offsets and decreases with increasing saturation for NAPL-1 and is almost constant with saturation for NAPL-2.

The reflection coefficients for different contaminant saturations and for the TM and TE cases are shown in Figs 7 and 8, where the absolute values of the reflection coefficients are displayed on the left-hand side and the respective phase angles on the right-hand side. The minima in the TM reflection coefficients correspond to the pseudo-Brewster angles (see Fig. 6). The type of TM (TE) anomaly is negative (positive) for all the saturations. At low NAPL saturations, the contrast is due to the difference between the dielectric constants of air and water. NAPL-2 produces the higher reflection coefficient at high saturations, because the high conductivity contributes to the effective permittivity, reaching a dielectric constant of 13. The saturation can be determined on the basis of the reflection strength only for the low-conductivity NAPL-1.

Next, we compute the TM and TE reflection coefficients for the LNAPL/water interface (model 4, lower interface). The results are shown in Figs 9 and 10, respectively. In this case, the pseudo-Brewster angle increases for increasing NAPL saturation. This feature, plus the reflection strength and phase angle are the main factors used to discriminate between the saturations. On the other hand, the reflection strength of TE waves shows little difference between NAPL-1 and NAPL-2, but the phase angles differ.

Finally, the water/DNAPL interface is considered. The results for the TM and TE coefficients are shown in Figs 11 and 12, respectively. In this case, pseudo-Brewster angles can be found at near offsets, but they are more difficult to detect than those corresponding to the air/NAPL interface, since the reflection event is affected by the presence of the upper interfaces. A pseudo-critical angle occurs after the pseudo-Brewster angle in the TM case. This feature is also present in the TE reflection coefficients. The difference between the NAPL-1 and NAPL-2 cases is significant after the pseudo-critical angle. A similar effect occurs in the viscoelastic case (Carcione *et al*. 1998). Beyond the critical angle, the normal component of the energy-flux vector vanishes in the lossless case, and there is no transmission to the lower medium. The energy travels along the interface and the plane wave is evanescent. In the lossy case, these effects disappear and the fluxes of the reflected and refracted waves have to counteract a non-zero interference flux. Since the flux of the refracted wave is always greater than zero, there is transmission for all the angles of incidence (Carcione 2001).

Regarding the dependence of the Fresnel coefficients as a function of frequency, we obtain similar qualitative trends in the GPR frequency band ranging from 10 MHz to 1 GHz, where the attenuation is almost constant (Davis and Annan 1989; Carcione 1996a).

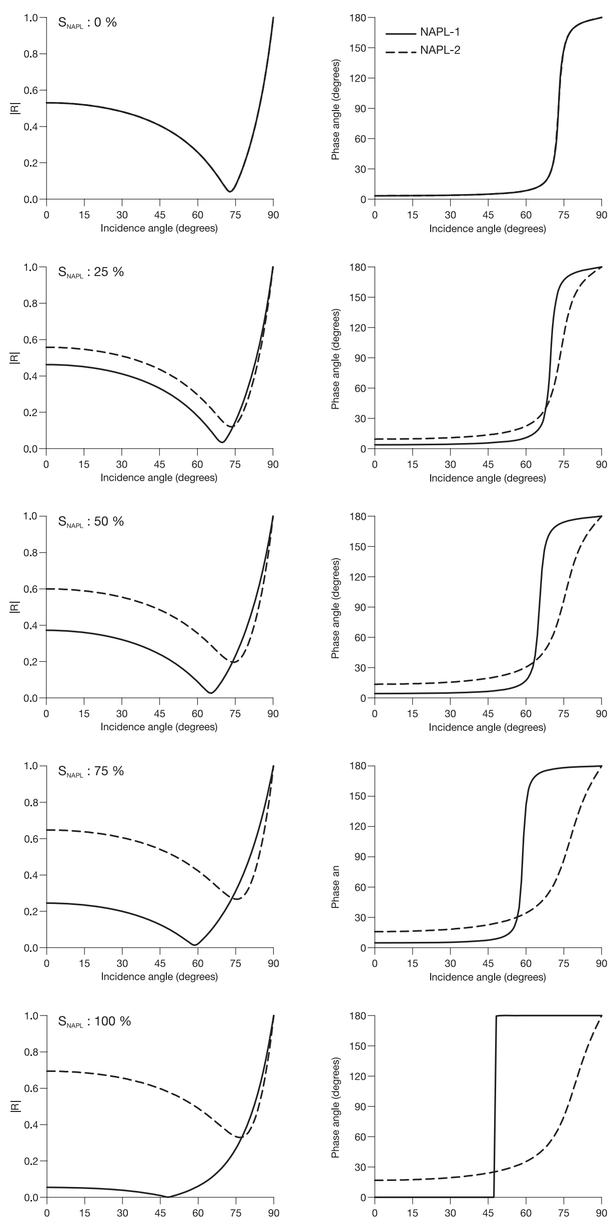

FIGURE 7

TM Fresnel coefficients for the dry soil/LNAPL interface (model 4, upper interface) and various NAPL saturations. The other saturating fluid is salt water. The left-hand column shows the absolute values and the right-hand column shows the respective phase angles.

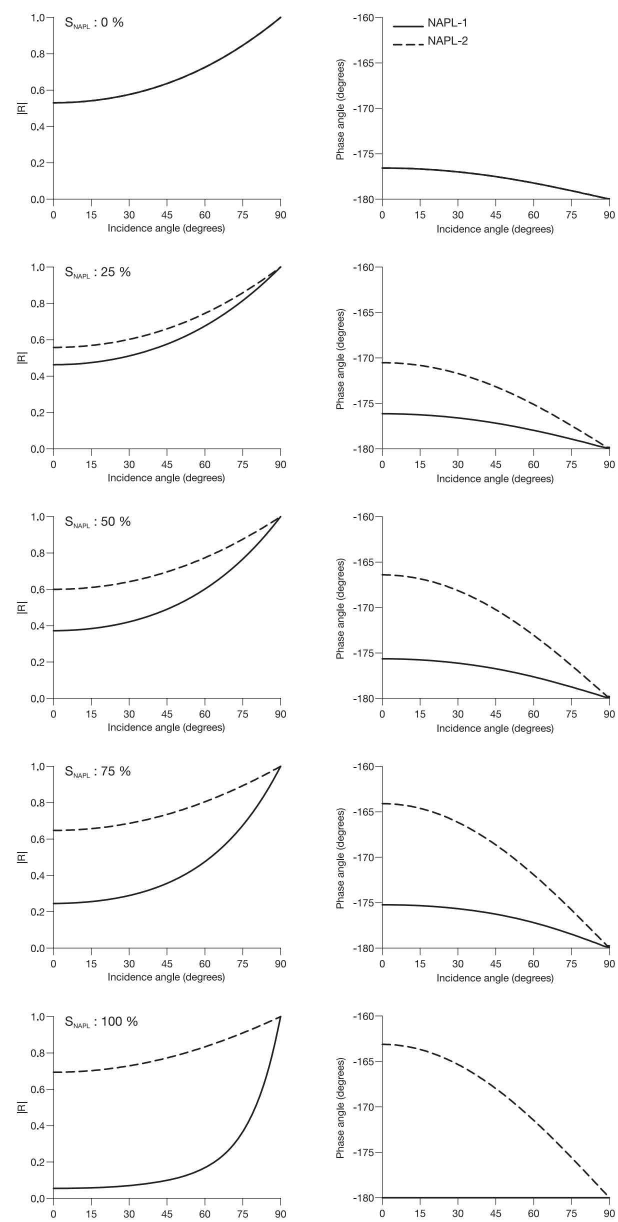

FIGURE 8

TE Fresnel coefficients for the dry soil/LNAPL interface (model 4, upper interface) and various NAPL saturations. The other saturating fluid is salt water. The left-hand column shows the absolute values and the right-hand column shows the respective phase angles.

AVA analysis from synthetic radargrams

In order to obtain the reflection coefficients from space–time domain data, we compute synthetic radargrams by using a domain-decomposition method to model the upper and lower media by using two grids (Carcione 1991, 1994) and the equation of motion for shear waves. This approach makes use of the mathematical analogy between SH waves, whose attenuation is described by the Maxwell viscoelastic model, and Maxwell's equations (Carcione and Cavallini 1995; Carcione 1996b) (see Appendix). The AVA analysis is performed with a method developed by Kindelan *et al*. (1989) for elastic media. This method has been applied with success to extract the reflection coefficient of the ocean-bottom in the presence of the viscoelastic Rayleigh-window phenomenon (Carcione and Helle 2004).

The AVA analysis consists on the following steps:

1 Generate a synthetic radargram of the electric field, placing a line of receivers at each gridpoint above the interface. This radargram contains the incident and reflected fields.
2 Compute the synthetic radargram without an interface (i.e. without the lower medium) at the same location. The radargram contains the incident field only.
3 Take the difference between the first and second radargrams. The difference contains the reflected field only.
4 Perform an (, k_x)-transform of the incident field to obtain E_0(, k_x), where is the frequency and k_x is the horizontal wavenumber.
5 Perform an (, k_x)-transform of the reflected field to obtain E(, k_x).

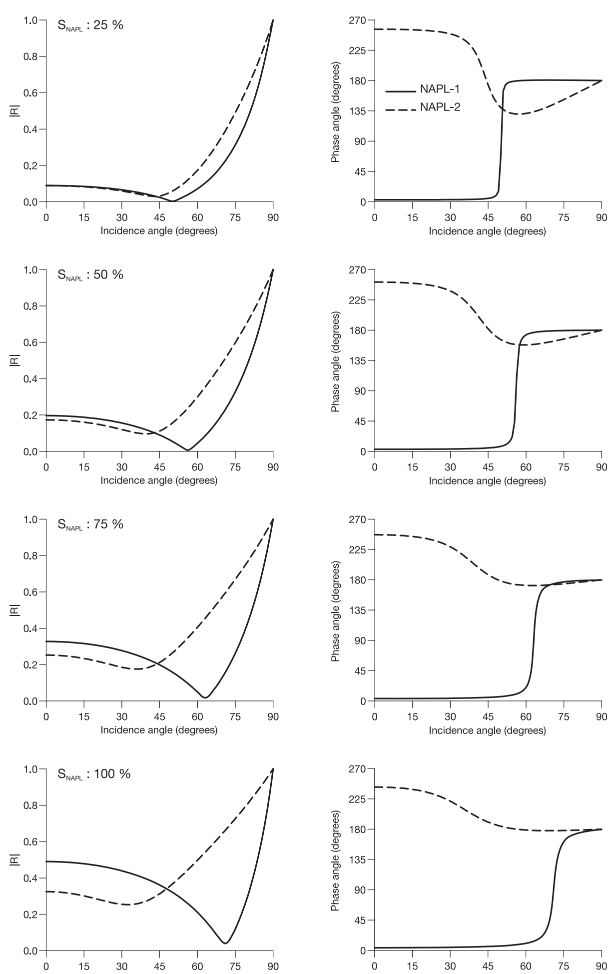

FIGURE 9

TM Fresnel coefficients for the LNAPL/water interface (model 4, lower interface) and various NAPL saturations. The other saturating fluid is salt water. The left-hand column shows the absolute values and the right-hand column shows the respective phase angles.

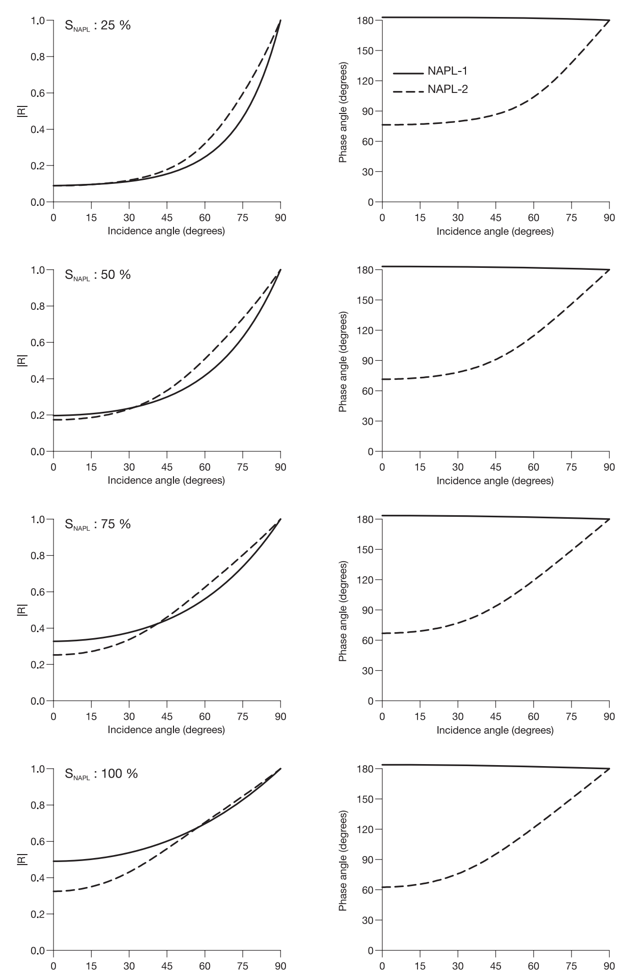

FIGURE 10

TE Fresnel coefficients for the LNAPL/water interface (model 4, lower interface) and various NAPL saturations. The other saturating fluid is salt water. The left-hand column shows the absolute values and the right-hand column shows the respective phase angles. The solid line corresponds to NAPL-1 and the dashed line to NAPL-2.

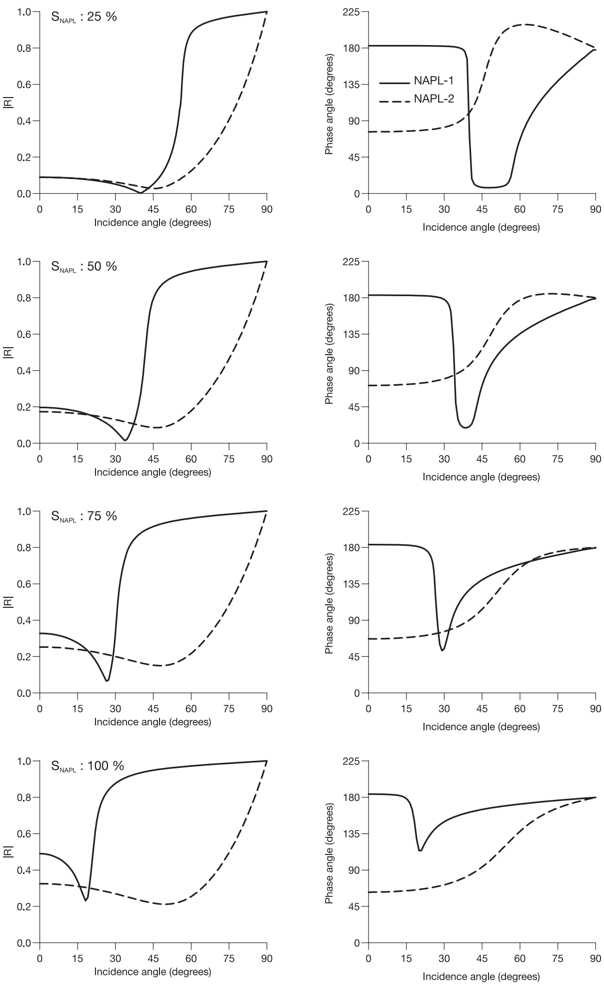

FIGURE 11

TM Fresnel coefficients for the water/DNAPL interface (model 5) and various NAPL saturations. The other saturating fluid is salt water. The left-hand column shows the absolute values and the right-hand column shows the respective phase angles.

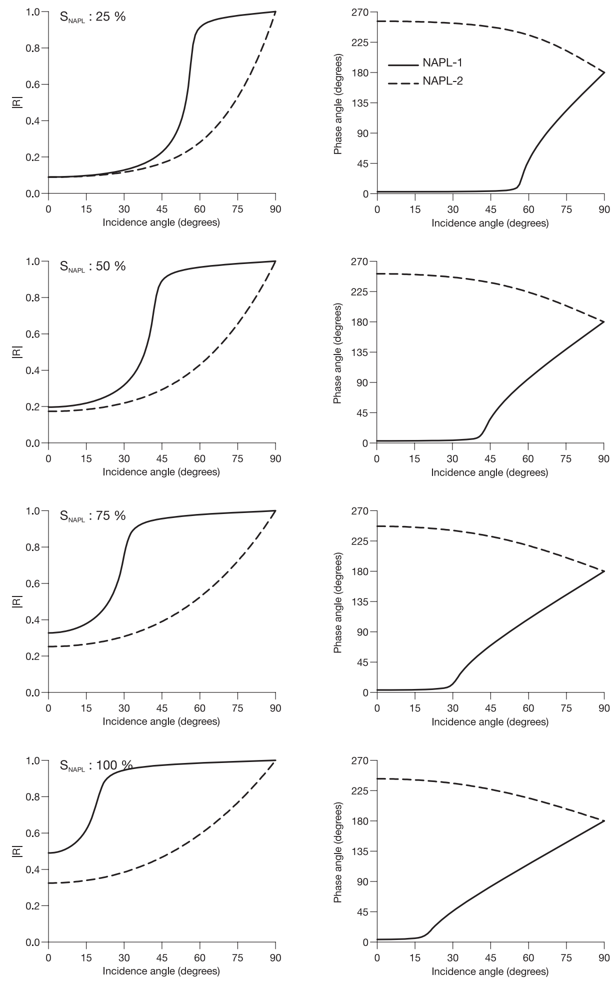

FIGURE 12

TE Fresnel coefficients for the water/DNAPL interface (model 5) and various NAPL saturations. The other saturating fluid is salt water. The left-hand column shows the absolute values and the right-hand column shows the respective phase angles.

6 Define $A = E(, k_x)/ E_0(, k_x)$; the quantity $|A|$ is the absolute value of the reflection coefficient, and the phase angle is given by arctan[Im(A)/Re(A)]. Then transform k_x to angle of incidence by using $\sin\ = v_{ph} k_x / w$, where v_{ph} is the phase velocity in the upper medium.

This is an outline of the method used by Kindelan *et al.* (1989). Knowledge of the incident field E_0 on the interface is necessary to correct for effects such as the antenna radiation pattern, polarization, and propagation effects due to the upper layers (the ‘overburden effects’). In the case of a single interface and a fairly homogeneous surface layer, E_0 can be obtained from the direct wave.

We consider the case with S_{NAPL} = 50% shown in Fig. 11. The lossless case – considering the real parts of the permittivities – has a Brewster angle at 34° and a critical angle at 43°. The modelling allows a maximum angle of incidence of approximately 80°. Beyond this angle, the traces are tapered by the absorbing boundary. Therefore, there is no need to taper the radargrams to compute the Fourier transform to the wavenumber domain. In this example, we do not model the surface of the earth, and therefore the radiation effects due to the presence of the surface. Thus, the data has to be preprocessed to obtain the incident field E_0 that takes into account the appropriate corrections (e.g. Zeng *et al*. 2000).

Figure 13 shows the comparison between (a) the lossless and (b) the lossy (the case in Fig. 11) reflection coefficients. The symbols correspond to the numerical evaluation for different frequencies (star: 90 MHz; circle: 100 MHz; triangle: 110 MHz) (the source central frequency is 100 MHz). The numerical evaluation of the phase angle is shown in Fig. 14. As can be seen, the method of estimation of the AVA response performs very well at the Brewster and critical angles.

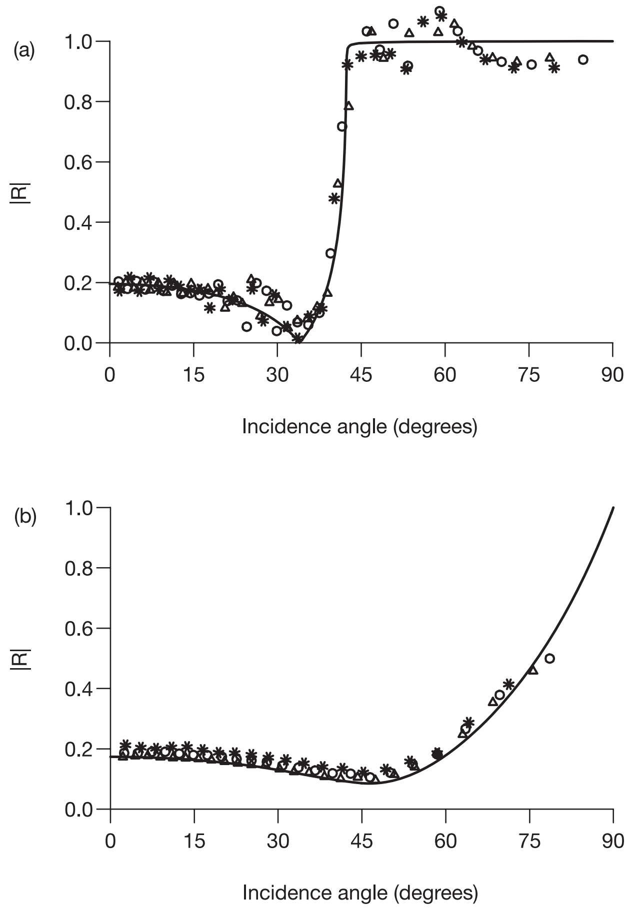

FIGURE 13
(a) Lossless and (b) lossy reflection coefficients versus angle of incidence for the TM case with S_{NAPL} = 50%, shown in Fig. 11. The symbols correspond to a numerical evaluation for different frequencies (star: 90 MHz; circle: 100 MHz; triangle: 110 MHz).

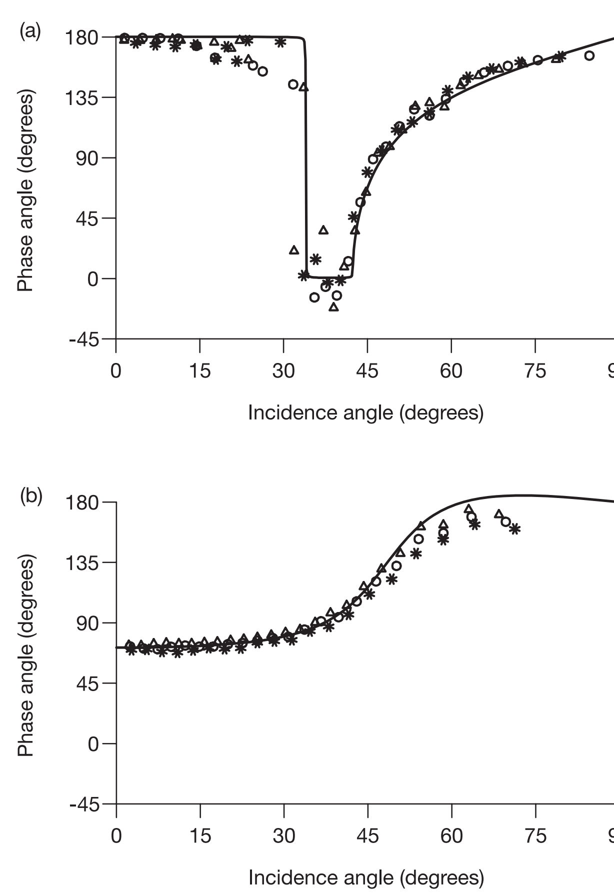

FIGURE 14
(a) Lossless and (b) lossy phase angle versus angle of incidence for the TM case with S_{NAPL} = 50%, shown in Fig. 11. The symbols correspond to a numerical evaluation for different frequencies (star: 90 MHz; circle: 100 MHz; triangle: 110 MHz).

CONCLUSIONS

We have computed the Fresnel reflection coefficients at GPR frequencies for the cases of fresh water interacting with seawater in coastal aquifers and floating hydrocarbons in the subsoil. The general common feature is that the TM mode (parallel polarization) has a negative anomaly and the TE mode (perpendicular polarization) has a positive anomaly. The advantage of using the TM-mode configuration is the presence of a pseudo-Brewster angle for relatively resistive media, which can be used to determine the NAPL saturation when the properties of the upper layer are known. At the top of the spill (air/LNAPL interface), this angle decreases with increasing saturation. The opposite effect occurs for the NAPL/water interface. In cases when the reflection strength cannot be used to discriminate between low- and high-conductivity NAPL, the interpretation can be based on the phase angles, which show significant differences.

The saturation can be determined on the basis of the reflection strength only for low-conductivity LNAPL (as above, knowing the upper-layer properties). The higher permittivity and conductivity for bio-degraded LNAPL causes a strong reflectivity of the top of the hydrocarbon plume and significant energy losses through the plume. This explains the characteristic response observed in radargrams of old (bio-degraded) hydrocarbon spills. When the type of anomaly and the reflection strength do not provide conclusive results, the traveltime of the reflection hyperbola can be used to obtain the characteristics of the upper medium. The main characteristic of the water/DNAPL interface is the presence of pseudo-Brewster and pseudo-critical angles. The increase in the magnitude of the reflection coefficient beyond the pseudo-critical angle is significant.

Finally, a wave-simulation algorithm and an AVA method are proposed for investigating and obtaining the pre- and post-critical reflection coefficients and phase angles. The AVA method is based on the wavenumber–frequency Fourier transform. Use of the – *p* transform to perform AVA is under investigation.

ACKNOWLEDGEMENTS

This work was financed in part by the European Union under the framework of the HYGEIA project, in part by Direzione Generale per la Promozione e la Cooperazione Culturale (Ministero degli Affari Esteri, Italy), and in part by Secretaría de Ciencia, Tecnología e Innovación Productiva (Ministerio de Educación, Ciencia y Tecnología, Argentina). We thank the Associate Editor, Prof. Evert C. Slob, and an anonymous reviewer for providing very useful comments.

REFERENCES

Baker G.S. 1998. Applying AVO analysis to GPR data. *Geophysical Research Letters* **25**, 397–400.

Benson A.K. 1995. Applications of ground penetrating radar in assessing some geological hazards: examples of groundwater contamination, faults, cavities. *Journal of Applied Geophysics* **33**, 177–193.

Born M. and Wolf E. 1964. *Principles of Optics*. Pergamon Press, Inc.

Botelho M.A.B., Machado S.L., Dourado T.C. and Amparo N.S. 2003. Experimentos laboratoriais com GPR (1 GHz) em corpos arenosos para analisar a influência da água e de hidrocarbonetos na sua velocidade de propagação. 8th International Congress of the Brazilian Geophysical Society, Rio de Janeiro, Brazil, Expanded Abstracts,

Carcione J.M. 1991. Domain decomposition for wave propagation problems. *Journal of Scientific Computing* **6**(4), 453–472.

Carcione J.M. 1994. The wave equation in generalized coordinates. *Geophysics* **59**, 1911–1919.

Carcione J.M. 1996a. Ground penetrating radar: wave theory and numerical simulation in conducting anisotropic media. *Geophysics* **61**, 1664–1677.

Carcione J.M. 1996b. Ground radar simulation for archaeological applications. *Geophysical Prospecting* **44**, 871–888.

Carcione J.M. 2001. *Wave Fields in Real Media. Theory and Numerical Simulation of Wave Propagation in Anisotropic, Anelastic and Porous Media*. Pergamon Press, Inc.

Carcione J.M. and Cavallini F. 1995. On the acoustic-electromagnetic analogy. *Wave Motion* **21**, 149–162.

Carcione J.M. and Helle H.B. 2004. On the physics and simulation of wave propagation at the ocean bottom. *Geophysics* **69**, 825–839.

Carcione J.M., Helle H. and Zhao T. 1998. The effects of attenuation and anisotropy on reflection amplitude versus offset. *Geophysics* **63**, 1652–1658.

Carcione J.M., Marcak H., Seriani G. and Padoan G. 2000. GPR modeling study of a contaminated area of Krzywa airbase (Poland). *Geophysics* **65**, 521–525.

Carcione J.M. and Seriani G. 2000. An electromagnetic modelling tool for the detection of hydrocarbons in the subsoil. *Geophysical Prospecting* **48**, 231–256.

Carcione J.M., Seriani G. and Gei D. 2003. Acoustic and electromagnetic properties of soils saturated with salt water and NAPL. *Journal of Applied Geophysics* **52**, 177–191.

Cole K.S. and Cole R.H. 1941. Dispersion and absorption in dielectrics. *Journal of Chemical Physics* **9**, 341–351.

Daniels J.J., Roberts R. and Vendl M. 1995. Ground penetrating radar for the detection of liquid contaminants. *Journal of Applied Geophysics* **33**, 195–207.

Davis J.L. and Annan A.P. 1989. Ground-penetrating radar for high-resolution mapping of soil and rock stratigraphy. *Geophysical Prospecting* **37**, 531–551.

Debye P. 1929. *Polar Molecules*. Dover, New York.

Greenhouse J., Brewster M., Schneider G., Redman D., Annan P., Olhoeft G., Lucius J., Sander K. and Mazzella A. 1993. Geophysics and solvents: The Borden experiment. *The Leading Edge* **12**(4), 261–267.

Kindelan M., Seriani G. and Sguazzero P. 1989. Elastic modelling and its application to amplitude versus angle interpretation. *Geophysical Prospecting* **37**, 3–30.

Knight R. and Endres A. 1990. A new concept in modeling the dielectric response of sandstones: Defining a wetted rock and bulk water system. *Geophysics* **55**, 586–594.

Lehmann F. 1996. Fresnel equations for reflection and transmission at boundaries between two conductive media, with applications to georadar problems. *Proceedings of the 6th International Conference on Ground Penetrating Radar, Sendai (Japan)*, pp. 555–560.

Lutz P., Garambois S. and Perroud H. 2003. Influence of antenna configurations for GPR survey: information from polarization and amplitude versus offset measurements. In: *Ground Penetrating Radar in Sediments* (eds C. Bristow and H.M. Jol), pp. 299–313. Geological Society, London.

Osella A., de la Vega M. and Lascano E. 2002. Characterization of a contaminant plume due to a hydrocarbon spill using geoelectrical methods. *Journal of Environmental and Engineering Geophysics* 7, 78–87.

Pereira A.J., Gambôa L.A.P., da Silva M.A.M., da Costa A. and Rodrigues A.R. 2003. Uso do GPR na identificação da interface água doce/água salgada em cordões arenosos da praia de Itaipuaçú - Municipio de Maricá (RJ). 8th International Congress of the Brazilian Geophysical Society, Rio de Janeiro, Brazil, Expanded Abstracts,

Reppert P.M., Morgan D.F. and Toksöz N.M. 2000. Dielectric constant determination using ground-penetrating radar reflection coefficients. *Journal of Applied Geophysics* **43**, 189–197.

Roberts R.L. and Daniels J.J. 1996. Analysis of GPR polarization phenomena. *Journal of Environmental and Engineering Geophysics* **1**, 139–157.

Sauck W.A. 2000. A model for the resistivity structure of LNAPL plumes and their environs in sandy sediments. *Journal of Applied Geophysics* **44**, 151–165.

Schön J.H. 1996. *Physical Properties of Rocks, Handbook of Geophysical Exploration*. Pergamon Press, Inc.

Taherian M.R., Kenyon W.E. and Safinya K.A. 1990. Measurement of dielectric response of water-saturated rocks. *Geophysics* **55**, 1530–1541.

de la Vega M., Osella A. and Lascano E. 2003. Joint inversion of Wenner and dipole-dipole data to study a gasoline-contaminated soil. *Journal of Applied Geophysics* **54**, 97–109.

Zeng X., McMechan G.A. and Xu T. 2000. Synthesis of amplitude-versus-offset variations in ground-penetrating radar data. *Geophysics* **65**, 113–125 .

APPENDIX

The domain-decomposition method for Maxwell's equation

We compute synthetic radargrams by using the equation of motion for shear waves, and modeling the upper and lower media with two grids, a procedure that is termed *domain decomposition* in computational acoustics and fluid dynamics. This type of modelling has been used extensively by one of the authors to model elastic waves (Carcione 1991, 1994; Carcione and Helle 2004).

Let us assume that the propagation is in the (x, z)-plane, and that the material properties are invariant in the y-direction. Then, E_x, E_z and H_y are decoupled from E_y, H_x and H_z. In the absence of electric source currents, the first three field components obey the TM (transverse magnetic field) differential equations:

$$\begin{aligned}
&\frac{\partial E_z}{\partial x} - \frac{\partial E_x}{\partial z} = \mu \frac{\partial H_y}{\partial t}, \\
&-\frac{\partial H_y}{\partial z} = \sigma E_x + \varepsilon \frac{\partial E_x}{\partial t} + J_x, \\
&\frac{\partial H_y}{\partial x} = \sigma E_z + \varepsilon \frac{\partial E_z}{\partial t} + J_z,
\end{aligned} \tag{A1}$$

where μ is the magnetic permeability, is the dielectric permittivity, is the conductivity and J denotes electric sources. Ignoring the source terms, (A1) can be recast as

$$\frac{\partial \mathbf{e}}{\partial t} = \mathbf{M} \cdot \mathbf{e} \equiv \mathbf{A} \cdot \frac{\partial \mathbf{e}}{\partial x} + \mathbf{B} \cdot \frac{\partial \mathbf{e}}{\partial z}, \tag{A2}$$

where $\mathbf{e} = (H_y, E_x, E_z)^T$, and $\mathbf{A}$ and $\mathbf{B}$ are matrices which depend only on the medium properties.

Carcione and Cavallini (1995) have established the mathematical analogy between SH and TM waves, where the former are shear waves polarized in the horizontal plane. In order to make use of the SH-wave modelling code, the equivalence is: H_y v_y, E_x $-_{yz}$, E_x $_{yz}$, μ and , where v and denote particle velocity and stress, G is the shear modulus, and is the density.

Two meshes model the upper and lower subdomains (labelled 1 and 2, respectively). The solution on each mesh is obtained by using the Runge–Kutta method as a time-stepping algorithm and the Fourier and Chebyshev differential operators to compute the spatial derivatives in the horizontal and vertical directions, respectively (Carcione 2001).

The method to implement the correct boundary condition at the interface is based on the following arguments. Compute the eigenvalues of matrix **B** at the optical (high-frequency) limit (they are $\pm 1/\sqrt{\mu\varepsilon}$ and 0). Compute the right eigenvectors of matrix **B**, such that they are the columns of a matrix **R**. Then, $\mathbf{B}=\mathbf{R}\cdot\mathbf{\Lambda}\cdot\mathbf{R}^{-1}$, with $\mathbf{\Lambda}$ being the diagonal matrix of the eigenvalues. The characteristics array is then $\mathbf{c} = \mathbf{R}^{-1}\cdot\ \mathbf{e}$. The wave equation has then been decomposed into decoupled incoming and outgoing waves, perpendicular to the interface (this decomposition results in the so-called *paraxial* wave equation). The non-zero characteristic variables for Maxwell's equations are explicitly given by

$$c_{\pm} = H_y \pm \frac{E_x}{I}, \quad I = \sqrt{\frac{\mu}{\varepsilon}}, \tag{A3}$$

where I is the electromagnetic impedance.

The explicit time-integration scheme used to solve (A2) computes the operation $\mathbf{M}\cdot\mathbf{e}\ (\mathbf{e})^{\mathrm{old}}$ at each time-step. At the interface separating the two meshes, the array $(\mathbf{e})^{\mathrm{old}}$ is then updated to give a new array $(\mathbf{e})^{\mathrm{new}}$ that takes the boundary conditions into account.

The boundary conditions imply continuity of E_x and H_y (Born and Wolf 1964), and this requires

$$\begin{aligned}
&E_x^{\mathrm{new}}(1) = E_x^{\mathrm{new}}(2) \equiv E_x^{\mathrm{new}}, \\
&H_y^{\mathrm{new}}(1) = H_y^{\mathrm{new}}(2) \equiv H_y^{\mathrm{new}}.
\end{aligned} \tag{A4}$$

The inward propagating waves depend on the solution outside the subdomains and therefore are computed from the boundary conditions, while the behaviour of the outward propagating waves is determined by the solution inside the subdomain. This requires $c_-^{\mathrm{new}}(1) = c_-^{\mathrm{old}}(1)$ and $c_+^{\mathrm{new}}(2) = c_+^{\mathrm{old}}(2)$, or

$$\begin{aligned}
&H_y^{\mathrm{new}} - \frac{E_x^{\mathrm{new}}}{I_1} = H_y^{\mathrm{old}}(1) - \frac{E_x^{\mathrm{old}}(1)}{I_1}, \\
&H_y^{\mathrm{new}} + \frac{E_x^{\mathrm{new}}}{I_2} = H_y^{\mathrm{old}}(2) + \frac{E_x^{\mathrm{old}}(2)}{I_2},
\end{aligned} \tag{A5}$$

where we have used the equations (A4).

The solution of this system of equations yields the boundary equations,

$$\begin{aligned}
&H_y^{\mathrm{new}} = \frac{1}{I_1 + I_2}\left[I_1 H_y^{\mathrm{old}}(1) + I_2 H_y^{\mathrm{old}}(2) - E_x^{\mathrm{old}}(1) + E_x^{\mathrm{old}}(2)\right], \\
&E_x^{\mathrm{new}} = \frac{I_1 I_2}{I_1 + I_2}\left[H_y^{\mathrm{old}}(2) - H_y^{\mathrm{old}}(1) + \frac{E_x^{\mathrm{old}}(2)}{I_2} + \frac{E_x^{\mathrm{old}}(1)}{I_1}\right].
\end{aligned} \tag{A6}$$

The remaining field variables satisfy $E_z^{\mathrm{new}}(1) = E_z^{\mathrm{old}}(1)$ and $E_z^{\mathrm{new}}(2) = E_z^{\mathrm{old}}(2)$.

© 2006 European Association of Geoscientists & Engineers,